JOURNAL OF MARINE RESEARCH

The *Journal of Marine Research,* one of the oldest journals in American marine science, published important peer-reviewed original research on a broad array of topics in physical, biological, and chemical oceanography vital to the academic oceanographic community in the long and rich tradition of the Sears Foundation for Marine Research at Yale University.

An archive of all issues from 1937 to 2021 (Volume 1–79) are available through EliScholar, a digital platform for scholarly publishing provided by Yale University Library at https://elischolar.library.yale.edu/.

Requests for permission to clear rights for use of this content should be directed to the authors, their estates, or other representatives. The *Journal of Marine Research* has no contact information beyond the affiliations listed in the published articles. We ask that you provide attribution to the *Journal of Marine Research.*

Yale University provides access to these materials for educational and research purposes only. Copyright or other proprietary rights to content contained in this document may be held by individuals or entities other than, or in addition to, Yale University. You are solely responsible for determining the ownership of the copyright, and for obtaining permission for your intended use. Yale University makes no warranty that your distribution, reproduction, or other use of these materials will not infringe the rights of third parties.

Descent of dense water masses along continental slopes

by Scott A. Condie[1,2]

ABSTRACT

The formation of dense water over the continental shelf and its descent along the continental slope have been investigated both theoretically and experimentally. Models have been developed for slope fronts and dense filaments, with emphasis on the role of the bottom boundary layer.

An analytical, two-layer, two-dimensional model is first presented for the development of dense slope fronts near the shelf-break. The effects of vertical viscosity are explored and two behavioral regimes identified. The most relevant regime is determined by the parameter $F = (U_Q/g\epsilon s)(f^3/\nu)^{1/2}$ where U_Q is the flux of newly created dense water per unit length of coastline, g is the gravitational acceleration, ϵ is the density anomaly, s is the bottom slope, f is the Coriolis parameter and ν is the vertical viscosity. In both cases, the alongslope velocity in the lower layer increases away from the coast during geostrophic adjustment, with an accompanying growth in the downslop Ekman flux. When F is small, dense water production near the coast can be balanced by transport within the boundary layer, which extends down the slope as a shallow intrusion with an alongslope speed of $g\epsilon s/f$. However, when F is large this type of flow cannot provide sufficient downslope transport. Dense water then accumulates, causing the front to steepen while diminishing the influence of the bottom slope. There is a corresponding increase in alongslope speed, which eventually plateaus at $(2f/\nu)^{1/2}/U_Q$ where the Ekman flux balances the production of new dense water. These behaviors are strongly supported by results from laboratory experiments and are consistent with the limited available observations of the Antarctic Slope Front.

After moving off the shelf, the dense water mass may continue to move down the slope within the bottom boundary layer, or alternatively, form an isolated filament with a front on both sides. Theoretical solutions are developed for dense filaments both with and without an active upper layer. In the latter case, the influence of dissipation is investigated beginning with a simple bulk parameterization. This produces a filament which broadens as it moves down the slope, while its mean alongslope velocity increases with bottom slope and its horizontal shear decreases. More realistic boundary layer dynamics have also been incorporated using a similar approach to that described for slope fronts. The solutions compare well with results from laboratory experiments on relatively stable filaments. Implications of the study for deep water formation around Antarctica are discussed briefly.

1. Research School of Earth Sciences, The Australian National University, Canberra, ACT 0200, Australia.

2. Present address: CSIRO, Centre for Environmental Mechanics, GPO Box 821, Canberra, ACT 2601, Australia.
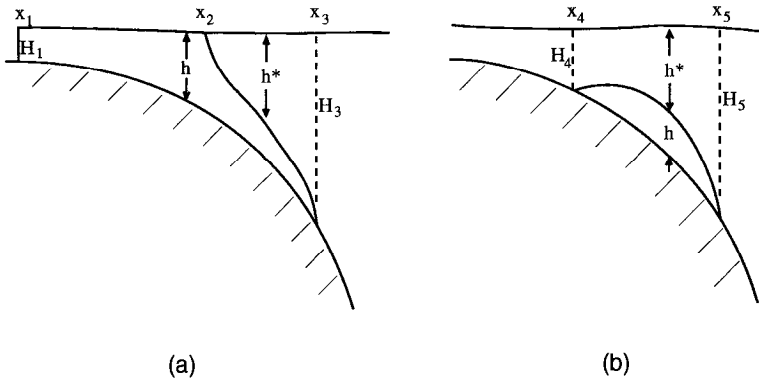
Figure 1. Schematic representations of (a) a slope front and (b) a dense filament bounded by a front.

1. Introduction

A major component of the ocean thermohaline circulation is the formation of dense water over the continental shelf and its descent down the continental slope into the deep ocean (Killworth, 1983). These processes may be initiated by sea-surface cooling, evaporation, ice formation or an influx of suspended sediments. The resulting flows take an important role in biogeochemical cycles by removing dissolved gases, nutrients, organic particles, sediments and pollutants from the coastal environment and replenishing deeper waters. Because it can take decades or more for the subducted water to resurface and interact with the atmosphere, such flows also provide a buffer to long term climatic variability. However, the convective processes responsible for deep and intermediate water formation along the continental margin are complex and poorly understood. They represent a source of major uncertainty in ocean circulation and coupled climate models, where they are usually represented by extremely simplistic parameterizations. To remedy this we must first develop an understanding of the fundamental fluid dynamical processes including the roles of bottom friction, mixing and shear instability. This study uses a combination of simple analytical theories and laboratory experiments to address some of these issues.

Deep water production along continental margins can be divided into three stages of development. The first is the production of dense water over the shelf which often results in the formation of a slope front separating dense shelf water from lighter water over the continental slope (Fig. 1a). If this occurs over a relatively large horizontal scale (~ 10 km), the influence of the earth's rotation will stop the dense fluid from cascading directly down the slope. Instead a geostrophic flow develops along the shelf, with downslope motions restricted to the bottom boundary layer. Further downstream, dissipation and topographic variations may cause the front to move off the shelf and down the continental slope. It then takes the form of a dense filament, separated from the environment by a bounded front (Fig. 1b). Eventually
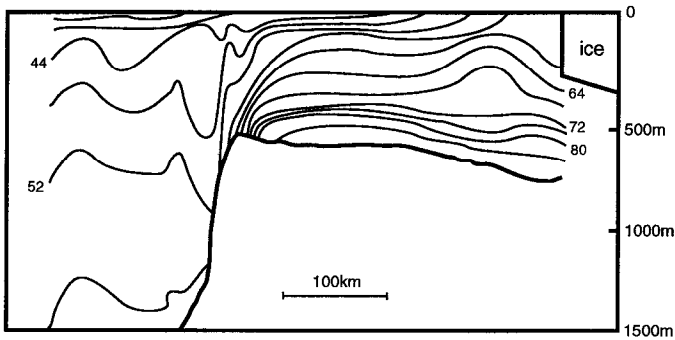
Figure 2. A vertical section of density ($\sigma_t + 32$, density relative to 1000 dbar) across the continental shelf and slope of the Ross Sea along 175W. Adapted from Jacobs (1991).

the filament reaches its own density level, where it may drive deep or intermediate circulation (Kawase, 1987; Condie and Kawase, 1993).

Examples of the features described in the previous paragraph are evident in many coastal regions where dense water is produced over the shelf at both large (Killworth, 1983) and smaller scales (Symonds and Gardiner-Garden, 1994). For example, subduction of newly formed Circumpolar Deep Water near the Antarctic shelf-break generates dense fronts in the Ross Sea (Jacobs *et al.*, 1970; Jacobs, 1991), further to the west off Wilkes Land (Carmack and Killworth, 1978) and along the Adelie Coast (Gordon and Tchernia, 1972). The Ross Sea example (reproduced in Fig. 2), has the general form of the surface-to-bottom slope front in Figure 1a, while the latter two have characteristics similar to the bounded front in Figure 1b. If these structures are typical of each of these locations, then they may represent the downstream development of a common subducting water mass.

Models of fronts near the shelf break have traditionally focused on the case of shelf water with density lower than that offshore. However, simple two-dimensional models for the formation of fronts of the form shown in Figure 1a have been developed by Hsueh and Cushman-Roisin (1983) and Ou (1983) for step and finite sloping topography respectively. They considered the inviscid geostrophic adjustment of a vertical front located at the shelf-break. A major limitation of this approach is the exclusion of any continuous sources of dense water production. Hence, there is no provision for the front to develop with time or distance downstream. However, these features have recently been included in an analytical frontal model with light shelf water (Condie, 1993) and can be extended to the case of dense shelf water.

The transition from a dense slope front into a filament is not well understood. Geostrophy should continue to be the dominant cross-stream balance throughout the transition and during the longer term development of the dense filament (Griffiths, 1986). However, inertia, bottom stress or mixing may be important in the

alongstream balance. Nof *et al.* (1991) retained inertial terms in their inviscid asymptotic theory of a bounded front. They explored the alongstream migration of the idealized front up and down the slope in response to varying topography and a planetary vorticity gradient.

A balance between bottom stress curl and vortex stretching also allows a front to migrate down the slope. This was first demonstrated by Smith's (1975) stream-tube model (solutions restricted to cross-stream integrated quantities) which has recently been applied to sedimentation problems (Wright *et al.*, 1990) and outflows with entrainment (Price and Baringer, 1994). Shaw and Csanady (1983) and Csanady (1988) also included bottom friction in a barotropic model based on Burger's equation, describing the spread of a dense blob on a sloping bottom. This was extended by Wright and Willmott (1992) to include baroclinic effects in a periodic domain, for application to the circumpolar ocean. The horizontal structure of dense filaments has also been resolved using a reduced gravity numerical model (Jungclaus and Backhaus, 1994), which gave good agreement with the earlier stream-tube results. The vertical cross-stream structure has been investigated numerically by Ezer and Weatherly (1990) using a two-dimensional primitive equation model. This study provided valuable insights into the detailed structure and influence of the bottom boundary layer.

Once a filament reaches its own density level, it forms a deep boundary current such as the Deep Western Boundary Current in the North Atlantic. This was first modeled by Stommel and Arons (1972) and recently extended by MacCready (1994) to explicitly include the dissipative effects of the bottom Ekman layer. MacCready (1994) neglected any interior stratification within the boundary current, which can generate buoyancy forces which oppose Ekman pumping down the slope (Mac-Cready and Rhines, 1991, 1993; Garrett *et al.*, 1993; Gawarkiewicz and Chapman, 1992; Chapman and Lentz, 1994). This effect should be less important for the flow geometries analyzed here (Fig. 1). With the possible exception of the upslope edge of the filament, buoyancy forces should act in the same direction as the Ekman pumping.

Both slope fronts and dense filaments may be modified by shear instability. This was first demonstrated by the laboratory experiments of Smith (1977), which revealed flow regimes ranging from quite viscous flow with large downslope flux, to meandering filaments which broke-up immediately into a string of eddies. Griffiths *et al.* (1982) later found that bounded fronts with an inertial alongstream balance are always linearly unstable and demonstrated this with laboratory experiments on the break-up of a light filament at a free surface. Thompson and Young (1989) and Nof (1990) then calculated the characteristics of similar eddy fields formed by the break-up of inviscid bottom filaments.

The present study uses analytical layered models to investigate the dynamics of dense fronts along the continental margins. The theoretical approach is similar to

that used previously by Stommel and Arons (1972), Griffiths (1986) and others. However, the current work uses two active layers and explicitly incorporates Ekman layer dynamics. Laboratory experiments have been used to substantiate the viscous scaling and identify additional effects associated with shear instability. An inviscid theory is developed for slope fronts in Section 2a. Ekman layer dynamics are included in Section 2b and compared to results from laboratory experiments in Section 2c. This sequence is then repeated for dense filaments in Section 3. Finally, some preliminary comparisons are made with observations over the Antarctic continental slope.

2. Slope fronts

The analysis of slope fronts begins with the geostrophic adjustment of a front separating two active layers of uniform potential vorticity. It will be demonstrated that in the inviscid case, the front responds to dense water production by migrating further offshore and increasing the lower layer velocity without limit. In Section 2b, it is shown how viscosity constrains the alongslope velocities and drives downslope transport within the Ekman layer. These ideas are then tested using simple laboratory experiments in Section 2c.

a. Geostrophic adjustment. Consider the slope front shown schematically in Figure 1a. The system rotates with angular velocity Ω and the topography has a bottom slope $s(x)$ where x is the offshore coordinate. Analytical solutions have been found for $s_{xx} = 0$. This includes not only the constant slope case ($s_x = 0$), but also slopes which increase in proportion to the distance offshore ($s_x = \alpha$ where α is a constant). The latter provides a good model of shelf-slope topography with continuous slope and is easily reproducible in the laboratory (Condie, 1993). The shore is located at $x = x_1$, where for simplicity it is assumed that the horizontal shear is negligible. A front separating immiscible fluids of densities ρ and ρ^* intersects the free surface at an outcropping point x_2 and the bottom at the leading edge x_3 The vertical momentum balance is hydrostatic, the cross-shelf balance is geostrophic and there are no along-shelf gradients.

The momentum equations in the dense lower layer are

$$fv = g[h_x - s] \qquad (x_1 < x < x_2), \tag{1}$$

$$fv = g[h_x + (1 - \epsilon)h_x^* - s] \qquad (x_2 < x < x_3), \tag{2}$$

and in the lighter upper layer

$$fv^* = g[h_x + h_x^* - s] \qquad (x_2 < x < x_3), \tag{3}$$

where h and h^* are the depths of the lower and upper layers, v and v^* are the respective along-shore velocities in these layers, $f = 2\Omega$ is the Coriolis parameter and $\epsilon = (\rho - \rho^*)/\rho$ is the density anomaly.

The boundary conditions are

$$h(x_1) = H_1, \tag{4}$$

$$h(x_3) = 0, \tag{5}$$

$$h^*(x_2) = 0, \tag{6}$$

$$h^*(x_3) = H_3, \tag{7}$$

$$v(x_1) = v_1, \tag{8}$$

$$v^*(x_3) = v_3, \tag{9}$$

with h and v continuous at x_2. The depth and velocity at the coast are denoted by H_1 and v_1 and at the offshore anchor point by H_3 and v_3. If the values of these quantities are given, then the values of x_3 and x_4 form part of the solution. Alternatively, if x_3 and x_4 are given, then either the coastal or offshore conditions form part of the solution.

Outside the bottom boundary layer, the frontal dynamics will be determined mainly by geostrophic adjustment. We can obtain solutions in the inviscid limit using potential vorticity conservation. If the dense fluid is formed near the coast where the depth is H_1, then this implies

$$v_x = f\left(\frac{h}{H_1} - 1\right). \tag{10}$$

If we define a characteristic depth H_* such that ligher layer fluid columns first enter the frontal region with potential vorticity f/H_*, then

$$v_x^* = f\left(\frac{h^*}{H_*} - 1\right). \tag{11}$$

The examples described below assume $H_* = h^*(x_3)$, so that upper layer fluid enters the frontal region with zero horizontal shear. However, H_* can be chosen to give any desired offshore shear.

It is convenient to first non-dimensionalize Eqs. (1) to (11) by scaling depths by H_1, cross-shelf distances by the barotropic deformation radius $(gH_1)^{1/2}/f$, velocities by the barotropic wave speed $(gH_1)^{1/2}$, and s by $f(H_1/g)^{1/2}$. This gives

$$v = h_x - s \qquad (x_1 < x < x_2), \tag{12}$$

$$v^* - v = \epsilon h_x^* \qquad (x_2 < x < x_3), \tag{13}$$

$$v^* = h_x + h_x^* - s \qquad (x_2 < x < x_3), \tag{14}$$

$$v_x = h - 1, \tag{15}$$

$$v_x^* = \frac{h^*}{H_*} - 1, \tag{16}$$

where Eq. (2) has been replaced by the Margules relation (13), obtained by combining Eqs. (2) and (3). Non-dimensionalization of (4) gives

$$h(x_1) = 1, \tag{17}$$

while the form of the remaining boundary conditions, (5) to (9), is unchanged. For later reference it is also noted that if the upper layer velocity is negligible, then Eqs. (13) and (14) combine to give geostrophy in its reduced gravity form,

$$v = \epsilon(h_x - s). \tag{18}$$

All quantities referred to in the remainder of the paper are non-dimensional unless otherwise stated.

Within the region $(x_1 < x < x_2)$ relations (12) and (15) give the hyperbolic equation,

$$h_{xx} - h = s_x - 1, \tag{19}$$

which has the general solution

$$h = c_1 e^x + c_2 e^{-x} - s_x + 1, \tag{20}$$

$$v = c_1 e^x - c_2 e^{-x} - s, \tag{21}$$

remembering that s_x is constant. Boundary conditions (17) and (8) then yield

$$c_1 = \tfrac{1}{2} e^{-x_1} [s_x + s(x_1) + v_1], \tag{22}$$

$$c_2 = \tfrac{1}{2} e^{x_1} [s_x - s(x_1) - v_1]. \tag{23}$$

Within the region $(x_2 < x < x_3)$ relations (13) to (16) give

$$h = \frac{h^*}{H_*} - \epsilon h^*_{xx} \tag{24}$$

and

$$\epsilon h^*_{xxx} - (1 + H_*^{-1}) h^*_{xx} + H_*^{-1} h^* = -s_x + 1. \tag{25}$$

Eq. (25) has the general solution

$$h^* = c_3 e^{k_3 x} + c_4 e^{-k_3 x} + c_5 e^{k_5 x} + c_6 e^{-k_5 x} - H_* (s_x - 1), \tag{26}$$

where

$$k_{3,5}^2 = \frac{1}{2\epsilon} \{ (1 + H_*^{-1}) \pm [(1 + H_*^{-1})^2 - 4\epsilon H_*^{-1}]^{1/2} \}. \tag{27}$$

It then follows from (24) that

$$h = K_3(c_3 e^{k_3 x} + c_4 e^{-k_3 x}) + K_5(c_5 e^{k_5 x} + c_6 e^{-k_5 x}) - s_x + 1, \qquad (28)$$

where $K_3 = H_*^{-1} - \epsilon k_3^2$ and $K_5 = H_*^{-1} - \epsilon k_5^2$. We now have expressions for the layer depths throughout the domain.

When (26) and (28) are substituted into (14) we obtain

$$v^* = k_3(K_3 + 1)(c_3 e^{k_3 x} - c_4 e^{-k_3 x}) + k_5(K_5 + 1)(c_5 e^{k_5 x} - c_6 e^{-k_5 x}) - s, \qquad (29)$$

and then from (13),

$$v = k_3(K_3 - \epsilon + 1)(c_3 e^{k_3 x} - c_4 e^{-k_3 x}) + k_5(K_5 - \epsilon + 1)(c_5 e^{k_5 x} - c_6 e^{-k_5 x}) - s. \qquad (30)$$

Applying boundary conditions (5) and (6) to (26) and (28) produces two linear equations for c_3 to c_6, while continuity of h and v at x_2 using (20) and (28), and (21) and (30) yields two more. The solution can be written in the matrix form

$$\begin{pmatrix} c_3 \\ c_4 \\ c_5 \\ c_6 \end{pmatrix} = \begin{pmatrix} e^{k_3 x_2} & e^{-k_3 x_2} & e^{k_5 x_2} & e^{-k_5 x_2} \\ K_3 e^{k_3 x_3} & K_3 e^{-k_3 x_3} & K_5 e^{k_5 x_3} & K_5 e^{-k_5 x_3} \\ K_3 e^{k_3 x_2} & K_3 e^{-k_3 x_2} & K_5 e^{k_5 x_2} & K_5 e^{-k_5 x_2} \\ k_3(K_3 - \epsilon + 1)e^{k_3 x_2} & -k_3(K_3 - \epsilon + 1)e^{-k_3 x_2} & k_5(K_5 - \epsilon + 1)e^{k_5 x_2} & -k_5(K_5 - \epsilon + 1)e^{-k_5 x_2} \end{pmatrix}^{-1}$$

$$\cdot \begin{pmatrix} (s_x - 1)H_* \\ (s_x - 1) \\ c_1 e^{x_2} + c_2 e^{-x_2} \\ c_1 e^{x_2} - c_2 e^{-x_2} \end{pmatrix}. \qquad (31)$$

The offshore flow conditions can then be obtained by applying boundary conditions (7) and (9) to (26) and (29),

$$H_3 = (1 - s_x)H_* + c_3 e^{k_3 x_3} + c_4 e^{-k_3 x_3} + c_5 e^{k_5 x_3} + c_6 e^{k_5 x_3}, \qquad (32)$$

$$v_3 = k_3(K_3 + 1)(c_3 e^{k_3 x_3} - c_4 e^{-k_3 x_3}) + k_5(K_5 + 1)(c_5 e^{k_5 x_3} - c_6 e^{-k_5 x_3}) - s(x_3). \qquad (33)$$

In principle, if the coastal and offshore boundary conditions are given, complete solutions including the values of x_2 and x_3 can now be determined numerically. However, it is much more convenient to specify x_2 and x_3 and calculate say the offshore conditions. c_3 to c_6 can be determined from (31) and substituted into relations (20), (21), (26), (28), (29) and (30) to provide explicit expressions for the layer depths and velocities throughout the domain.

Example solutions are shown in Figure 3 for shelf-slope topography characterized by $s = \alpha x$. The fronts tend toward an S-shape, with both layers characterized by anticyclonic shear due to the compression of fluid columns. The conditions are identical in 3a and 3b except that the front in the latter has been forced further offshore. This might occur in response to dense water production near the coast. As the front migrates offshore, lower layer velocities near the anchor point increase in
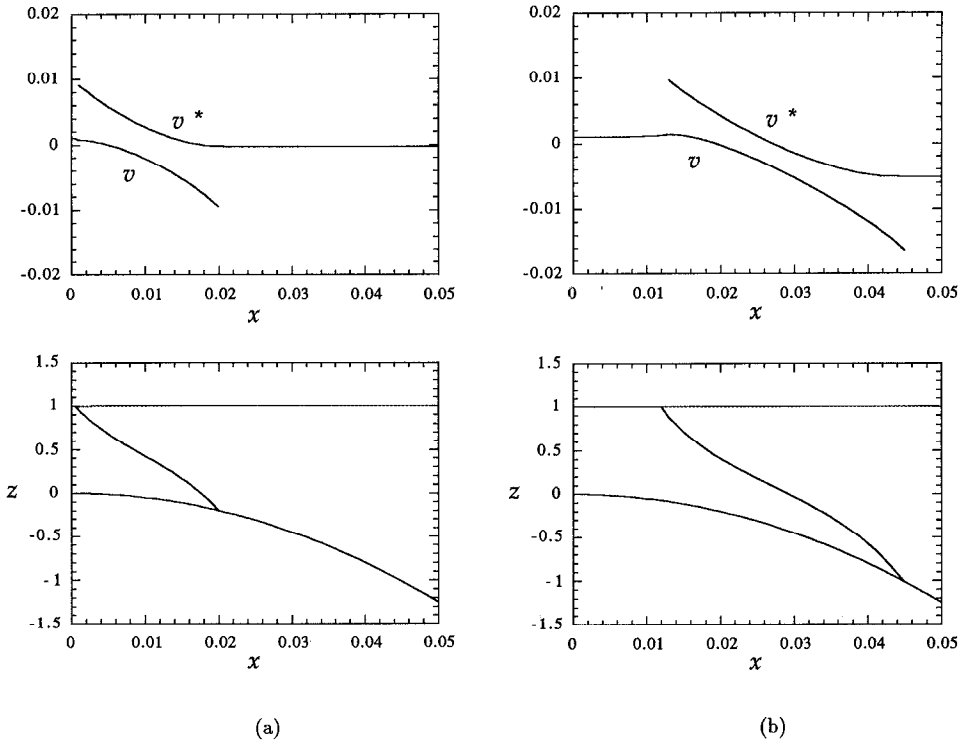
Figure 3. Inviscid slope front solutions for $\epsilon = 10^{-4}$, $\alpha = 10^3$, $x_1 = 0$, $v_1 = 10^{-3}$ and (a) $v_3 = -10^{-4}$, $H_* = H_3 = 1.2$, (b) $v_3 = 5 \times 10^{-3}$, $H_* = H_3 = 2.0$. The horizontal axis can be changed to units of internal deformation radii by multiplying by $\epsilon^{-1/2} = 100$. Note that the lower layer velocity near the anchor point increases in magnitude as the front moves further offshore.

magnitude. The Margules relation (13) then requires larger negative velocities in the upper layer. However, if v_3 is independently set by offshore processes, then the inviscid front is effectively trapped at a location consistent with this value. Eventually this solution must break down with the production of additional dense water. At this point ageostrophic processes such as vertical viscosity become important and must be incorporated into the solution.

b. Effects of viscosity. The increase in velocity magnitudes associated with the production of new dense water (Fig. 3) clearly cannot continue indefinitely. As we approach the leading edge where the lower layer thins, vertical viscosity becomes increasingly important and potential vorticity conservation ceases to be a good approximation. Velocities are then determined by the dynamics of the Ekman boundary layer, which pumps dense fluid down the slope. In particular, if the flow is steady and the dense water production rate is constant, then the Ekman flux which

builds up over the sheared geostrophic adjustment region must ultimately balance the flux of newly created dense water.

The structure of the viscous region of the flow is dependent on the local layer depth. If this is much greater than the Ekman boundary layer thickness and the bottom slope is less than the slope of the front, then the Ekman layer structure is essentially the same as that over flat topography (Pedlosky, 1987, p. 266). The downslope Ekman transport, non-dimensionalized by $(gH_1^3)^{1/2}$, is then given by $U_E = -(E/2)^{1/2}v$ where

$$E = \frac{\nu}{H_1^2 f}, \tag{34}$$

is the Ekman number and ν is the vertical viscosity coefficient of the lower layer. While ν continues to represent the velocity outside the boundary layer, the downslope velocity (scaling as $u_E = U_E/\delta_E$) is concentrated within a boundary layer of non-dimensional thickness $\delta_E = (2E)^{1/2}$ (Pedlosky, 1987, p. 192). Equating U_E with transport from the source U_Q, then yields alongslope and downslope velocity scales of

$$v_E = -2u_E = -\left(\frac{2}{E}\right)^{1/2} U_Q, \tag{35}$$

where U_Q has also been non-dimensionalized by $(gH_1^3)^{1/2}$.

Since the alongslope velocity is outside the boundary layer, it will continue to be geostrophic. In principle therefore, Eq. (35) could replace potential vorticity conservation in the lower layer (Eq. 15), allowing viscous solutions to be obtained for the two-layer system. However, the role of viscosity can be more easily investigated using the simpler reduced gravity system in which the upper layer velocity is assumed to be small. It is then straightforward to derive the geostrophic adjustment part of the solution from Eqs. (15) and (18). Eq. (18) can also be combined with (35) to obtain an expression for the layer depth in the viscous region,

$$h = -\left(\frac{2}{E}\right)^{1/2} \frac{U_Q}{\epsilon} (x - x_E) + \int_{x_E}^{x} s dx + h(x_E), \tag{36}$$

where $x = x_E$ is the offshore distance at which the viscous solution takes over from the geostrophic adjustment solution and $h(x_E)$ is given by Eq. (28).

Solutions (35) and (36) for the viscous region of the slope front can easily be matched with geostrophic adjustment solutions, which are represented by the solid curves in Figure 4. The viscous solutions represented by the dashed curves were obtained as follows. If U_Q and E are known, then matching v_E with the geostrophic adjustment velocity, gives the point x_E at which vertical viscosity becomes important. Eq. (36) then defines h for the region offshore of x_E. Figure 4a demonstrates how viscosity limits the alongslope velocity in the lower layer and extends the leading edge
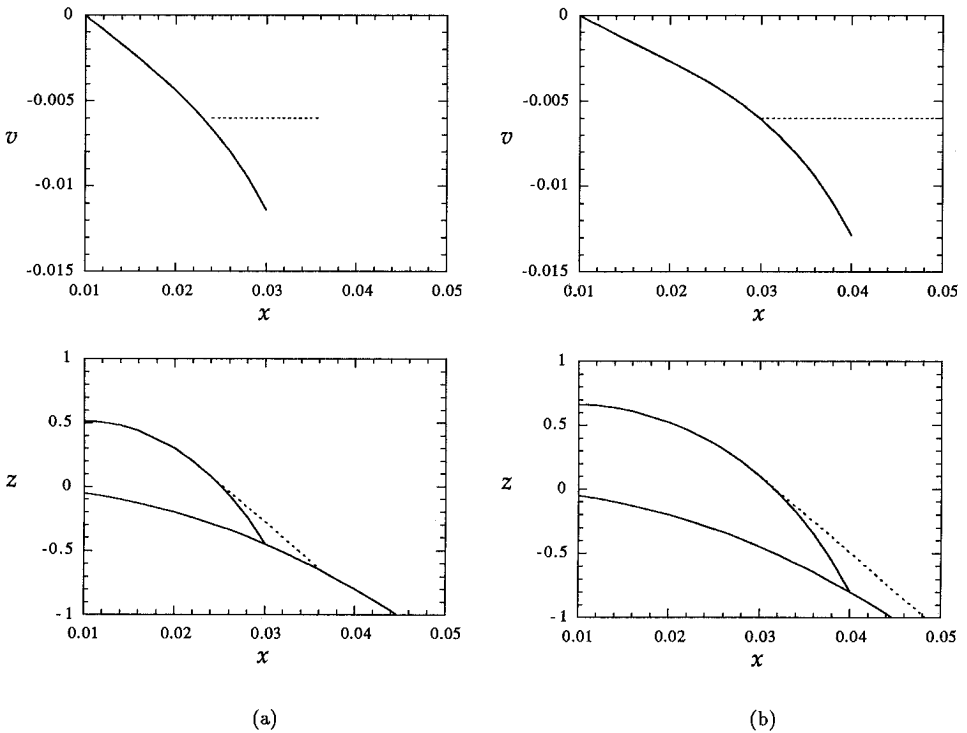
Figure 4. Slope front solutions with negligible upper layer velocity, $\epsilon = 10^{-4}$ and $\alpha = 10^3$. The dashed curves represent deviations from the inviscid geostrophic adjustment solutions associated with vertical viscosity characterized by $v_E = -(2/E)^{1/2}U_Q = -6 \times 10^{-3}$ and $F > 1$. The boundary conditions for the geostrophic adjustment part of the solution are $v = 0$ at $x = 0.01$ and (a) $x_3 = 0.03$, (b) $x_3 = 0.04$.

downslope. However, for non-zero source flux, both x_2 and x_E must continue to migrate offshore until the leading edge reaches its own density level or the interface becomes parallel to the bottom, as demonstrate by Figure 4b.

The viscous solutions described above tend to break down when the layer depth is comparable to the boundary layer thickness. Under these circumstances, the along-slope velocity is an integral part of the boundary layer solution and the bottom slope has a major influence on the flow structure. This problem is greatly simplified by noting that a necessary condition for a shallow layer to extend across a wide section of slope is that $h_x \ll s$. The geostrophic relation (18) then suggests an alongslope velocity scale of

$$v_N = -\epsilon s. \tag{37}$$

The subscript N refers to Nagata *et al.* (1993) who gave a detailed viscous solution for this limit. Their Figure 13 indicates that the downslope transport can be approxi-

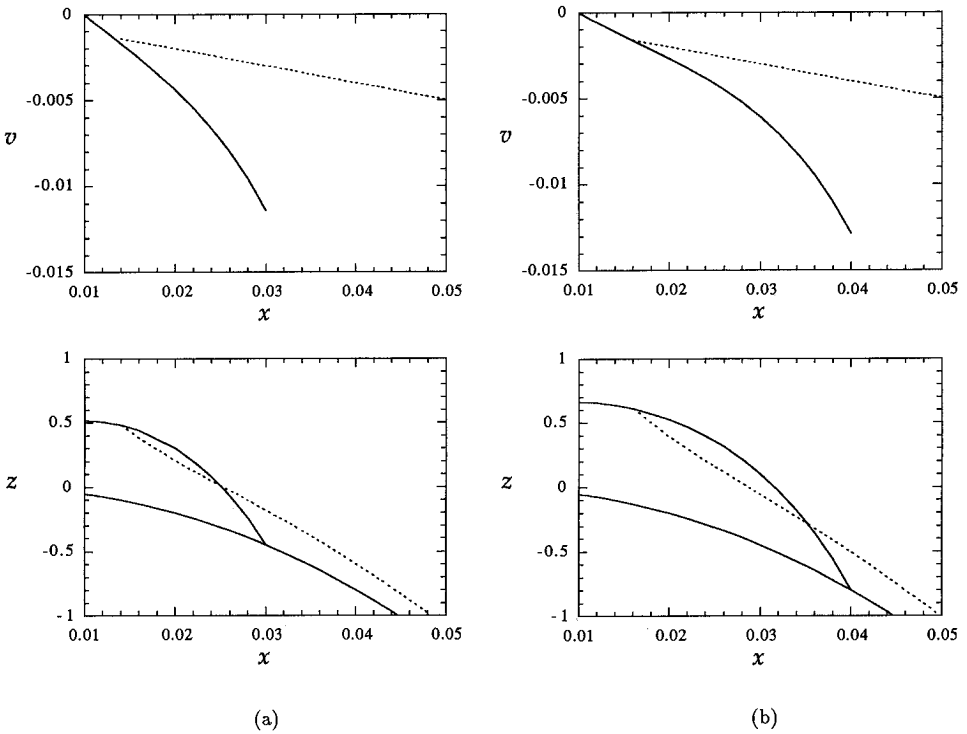(a)   (b)

Figure 5. As in Figure 4, except that the dashed curves represent deviations from the inviscid geostrophic adjustment solutions associated with vertical viscosity in a shallow layer with $F < 1$. (a) $U_Q = 2.2 \times 10^{-4}$ and $E > 2.6 \times 10^{-2}$. (b) $U_Q = 3.3 \times 10^{-4}$ and $E > 4.2 \times 10^{-2}$.

mated by $U_N = v_N h/3$ for $h < 3\delta_E/\sqrt{2}$, leveling off at a constant value of around $v_N \delta_E/\sqrt{2}$ for larger h. Equating this with the source flux and utilizing (37) we obtain,

$$h = \frac{3U_Q}{\epsilon s} < \frac{3\delta_E}{\sqrt{2}}. \qquad (38)$$

This is satisfied provided the ratio,

$$F = \frac{U_Q}{E^{1/2}\epsilon s}, \qquad (39)$$

satisfies $F < 1$.

Eqs. (38) and (39) define the velocity and layer depth profiles which can then be matched with inviscid profiles at a point, say x_N, at which viscosity becomes important. In Figure 5, the shallow layer solutions (dashed curves) are matched to the geostrophic adjustment solutions from Figure 4 (solid curves). In contrast to the previous scaling (Eqs. 35 and 36), each inviscid solution can only be matched to a
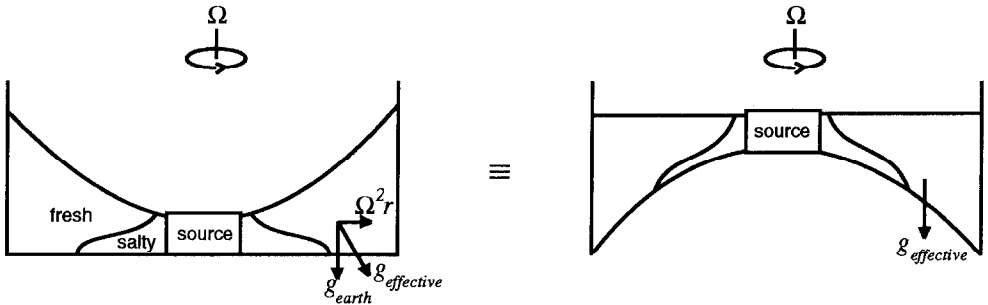
Figure 6. Side view of the axisymmetric configuration used in the slope front laboratory experiments. The right-hand figure shows the equivalent topography produced by centrifugal acceleration.

viscous solution with a particular value of U_Q. U_Q therefore uniquely determines both the geostrophic adjustment and viscous parts of the solution. This also differs from previous solutions in that the dense layer extends arbitrarily far down the slope, irrespective of the extent of the inviscid part of the flow. Both the increase in alongslope velocity and decrease in layer depth with distance offshore, are associated with the change in bottom slope.

For $F > 1$, the source flux exceeds the downslope transport U_N that can be carried by the shallow layer. Nagata *et al.* (1993) suggested that the flow must then be unsteady with dense fluid accumulating near the source without affecting the downslope flow. However, these conditions clearly cannot be sustained indefinitely. A more consistent scenario for $F > 1$ is that accumulation of source fluid increases the layer depth and steepens the front until the more traditional Ekman scaling takes over. Transitions between the two regimes can also occur where the bottom slope is changing. In Figure 4 for example, $F > 1$ for all $x > 0.043$, so strictly speaking there should be a transition to the shallow layer behavior at this point.

We can summarize the results of this section by noting that scales (37) and (38) can be applied over slope regions with $F < 1$, while (35) and (36) can be applied over regions with $F > 1$. The validity of these scales will now be tested using results from laboratory experiments.

c. Laboratory experiments. The laboratory experiments were conducted on a rotating table, utilizing an axisymmetric geometry to eliminate complex end effects. The configuration used to generate dense slope fronts is shown in Figure 6. A circular source of salty water was situated at the center of a cylindrical rotating tank containing fresh water. The bottom of the cylinder was horizontal. However, with rapid rotation, centrifugal accelerations distorted isopotentials in such a way that the gradient in fluid depth increased linearly with radius (Fig. 6). Nagata *et al.* (1993) conducted similar experiments using a conical bottom of uniform slope. Their study

focused on the small F regime and the results will be integrated with those from the current experiments to cover a wider range of parameters and behaviors.

When dense fluid was supplied continuously at the source, a front formed and spread radially away from the source. This was tracked by dying the dense fluid (Fig. 7a). The radial velocity component at later times could be determined by adding a different colored dye to the dense fluid. The alongslope velocity component was measured by streaklines originating from radially distributed dye sources within the lower layer (Fig. 7b). Velocity information within the upper layer was provided by video recordings of floating particles. The downslope component of the flow associated with Ekman pumping is directly evident in Figure 7b. The flows were also much more stable than those produced at the free surface under similar conditions (Condie, 1993), suggesting that the Ekman layer had a strong stabilizing influence.

Examples of the downslope and alongslope velocity profiles are shown in Figure 8. After the initial transient leading edge passed, these profiles remained relatively constant in both layers. The downslope velocity increased with radius, r, as fluid from the source accelerated anticyclonically along the slope. This may have been further magnified by concentration of the downslope transport into a thinning layer during geostrophic adjustment. However, both velocity components then fell away quite rapidly with radius. The trends in the upper layer were very similar close to the source where the layer depth was small and interfacial drag predominated. However, a weak anticyclonic shear consistent with geostrophic adjustment was evident at larger radii.

While the lower layer shear close to the source is qualitatively consistent with geostrophic adjustment, viscosity is clearly important over most of the flow where the velocity actually decays with radius. Ekman transports based on measured downslope velocities (Fig. 9a) and measured alongslope velocities (Fig. 9b) have been plotted against the transport from the source in accordance with relation (35). The dimensional form of the Ekman transport is $U_E = (2f/\nu)^{1/2}U_Q$, where the dense fluid transport is given by $U_Q = Q/2\pi r$ for the cylindrical geometry, Q being the total volume flux from the source. While significant scatter is evident in Figure 9 (discussed below), the results support the scaling and consistently indicate that around half of the source flux is carried within the Ekman layer.

The graphs in Figure 9 reveal that deviations from the theoretical scaling tend to occur either close to the source or under conditions of high Q and small ϵ, and therefore large F. In the first instance, the anomalously low Ekman transports near the source occur because radial transport is carried over the full layer depth during the geostrophic adjustment close to the source. In the second case, the weak dependence on Q and ϵ is due to the influence these parameters have on mixing. When $F > 10$ strong detrainment into the upper layer was observed close to the source. This reduces the radial flux which needs to be carried by the Ekman transport, thereby decreasing u and v.
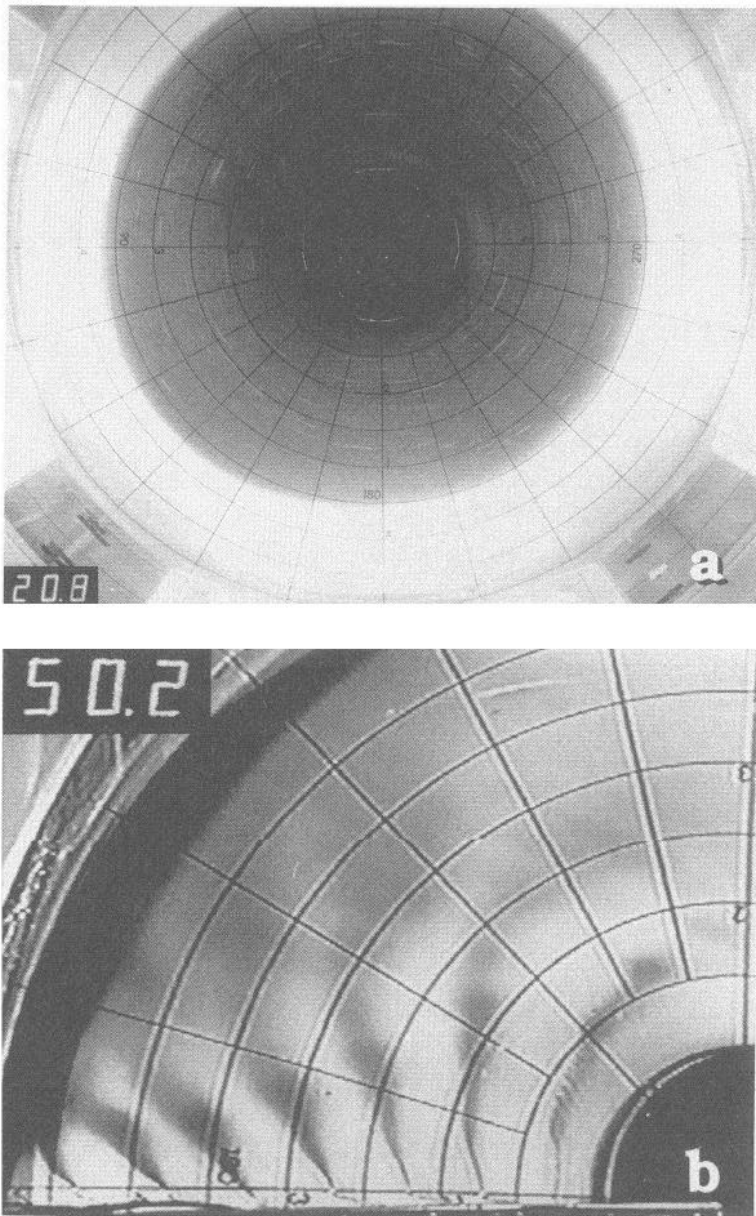
Figure 7. Axisymmetric slope fronts formed by the intrusion of dense water. (a) A two-second exposure taken 20 rotation periods after the source was turned on. The dense fluid is dyed and the streaks are produced by floating particles. The flow conditions were $H_1 = 1.0\,\text{cm}, f = 4.0\,\text{s}^{-1}$, $Q = 12.5\,\text{cm}^3\,\text{s}^{-1}$ and $\epsilon = 4.1 \times 10^{-2}$. (b) Dyed streaklines within the dense lower layer of the slope front 50 rotation periods after the source was turned on. The azimuthal velocity decreases with r so that the radial velocity component associated with Ekman pumping becomes more evident at large r.
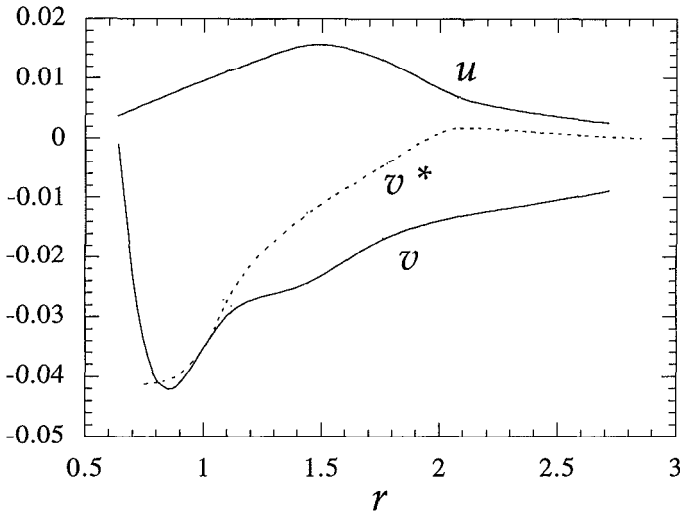
Figure 8. An example of downslope and alongslope velocity profiles from the laboratory slope fronts. These were measured approximately 18 rotation periods after the source of dense water was turned on. The radius has been non-dimensionalized by $(gH_1)^{1/2}/f$ and the velocities by $(gH_1)^{1/2}$ as in the theoretical figures. The conditions were $H_1 = 1.0$ cm, $f = 2.0$ s^{-1}, $Q = 12.5$ cm^3 s^{-1} and $\epsilon = 9.1 \times 10^{-2}$. Multiply the x-axis by $\epsilon^{-1/2} = 3.3$ to obtain units of internal deformation radii.

While these experiments are mostly characterized by relatively large values of F, there is some evidence in Figure 9 that the Ekman scaling also begins to break down as $F \to 1$. Furthermore, Nagata *et al.* (1993) note that their shallow layer solution is in quite good agreement with their laboratory results at low rotation rates (i.e. small F) and breaks down at higher rotation rates. These findings are consistent with our theoretical analysis which suggests that there should be a transition from the shallow layer solution to the more traditional Ekman solution at around $F = 1$. This is most clearly demonstrated by Figure 10, in which velocities from the current series of experiments and a selection covering the parameter range of Nagata *et al.*'s. experiments are plotted against F. Despite differences in the shape of the two topographies, the combined data reveal a fairly continuous transition between the two regimes. The traditional Ekman scaling works well for $F > 1$, although the influence of mixing is again evident for $F > 10$.

The implication of the laboratory results for ocean slope fronts is that bottom friction will limit the offshore migration and alongslope velocities associated with geostrophic adjustment, while enhancing the offshore transport within the boundary layer. If the production of dense water is small enough to satisfy $F < 1$, then it will be carried down the slope within a thin layer described by Eqs. (37) and (38). For higher production rates satisfying $F > 1$, the flow is described by Eqs. (35) and (36). While this provides a solid dynamical framework from which to interpret observations, its
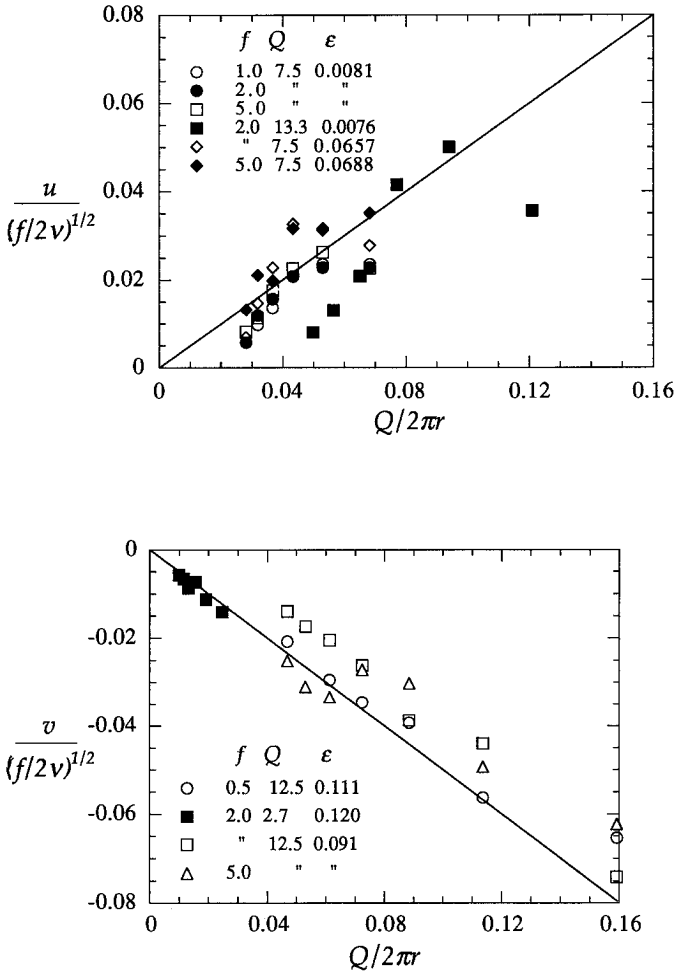
Figure 9. Ekman transport based on (a) measured downslope velocities and (b) measured alongslope velocities, plotted against the transport from the source.

use as a predictive tool is limited by our ability to estimate turbulent diffusivities ν and quantify other mixing processes which may be present at real ocean fronts.

It is also important to note that the viscous theories only strictly apply if the source flux is steady. For example, the laboratory experiments revealed that if the source was turned off after some time ($U_Q = 0$), the Ekman transport continued to remove dense fluid from the upper slope until its entire volume was transformed into a thin viscous bottom flow which spread slowly down the slope. Only then did the dense water mass completely separate from the source region. It therefore appears that the transition of a slope front over relatively flat topography into a dense filament requires more than the action of bottom friction alone. Presumably alongshore
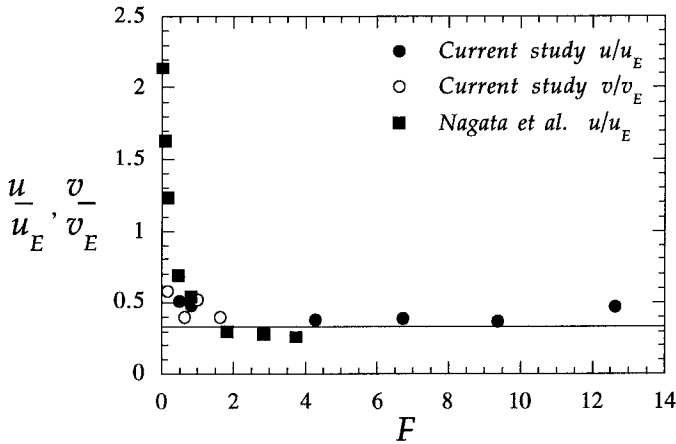
Figure 10. Downslope and alongslope velocities, non-dimensionalized in accordance with Eq. (35) and plotted against F. The solid squares have been replotted from the study of Nagata *et al.* (1993).

gradients in either the topography or the dense water production rate must also be present.

3. Dense filaments

Downstream from the dense water source, alongslope gradients in forcing or topography, combined with frictional effects in the alongstream momentum balance, may eventually move the front down the slope and away from the coast. It will then form a dense filament which intersects the bottom at two points (Fig. 1b). Vertical viscosity is again likely to play a strong role in the dynamics of these flows. After deriving inviscid solutions, the influence of both a simple bulk friction parameterization and more realistic Ekman layer dynamics will be examined. The latter reveals how dense fluid is pumped out of the filament and down the slope within the bottom Ekman layer. This behavior is confirmed by laboratory observations.

a. Two-layer geostrophic adjustment. To calculate a solution we will again assume that the flow is hydrostatic, geostrophic in the cross-stream direction, and has uniform potential vorticity. Solutions (26), (28), (29) and (30) for the layer depths and velocities can therefore be carried over from Section 2. However, when combined with the new boundary conditions:

$$h(x_4) = 0, \tag{40}$$

$$h(x_5) = 0, \tag{41}$$

$$h^*(x_4) = H_4, \tag{42}$$

$$h^*(x_5) = H_5, \tag{43}$$

they yield a new set of constants

$$
\begin{pmatrix} c_3 \\ c_4 \\ c_5 \\ c_6 \end{pmatrix} = \begin{pmatrix} e^{k_3x_4} & e^{-k_3x_4} & e^{k_5x_4} & e^{-k_5x_4} \\ e^{k_3x_5} & e^{-k_3x_5} & e^{k_5x_5} & e^{-k_5x_5} \\ K_3e^{k_3x_4} & K_3e^{-k_3x_4} & K_5e^{k_5x_4} & K_5e^{-k_5x_4} \\ K_3e^{k_3x_5} & K_3e^{-k_3x_5} & K_5e^{k_5x_5} & K_5e^{-k_5x_5} \end{pmatrix}^{-1} \begin{pmatrix} H_4 + (\alpha - 1)H_* \\ H_5 + (\alpha - 1)H_* \\ (\alpha - 1) \\ (\alpha - 1) \end{pmatrix}. \qquad (44)
$$

To close the problem we need to be given x_4 and x_5 or alternatively, be able to determine them from the upper layer velocities $v^*(x_4)$ and $v^*(x_5)$ using Eq. (29). The cross-sectional area beneath the front can also be found by integrating (15),

$$
\int_{x_4}^{x_5} h \, dx = x_5 - x_4 + v(x_5) - v(x_4). \qquad (45)
$$

An example of a two-layer dense filament solution is shown in Figure 11a. It is assumed that $H_* = H_5$, so that there is zero horizontal shear in the upper layer at x_5. Anticyclonic shear is generated by compression of fluid columns in both layers. However, the magnitude of this effect decreases with increasing upper layer depth. The horizontal shear in the lower layer is insensitive to the filaments location on the slope. However, solutions for fronts further offshore (not shown) reveal that the velocity becomes increasingly unidirectional and negative as Coriolis accelerations increase to balance the larger bottom slope.

b. *Deep filaments with dissipation.* A particularly simple solution can be found for dense filaments which reach a sufficient depth that any motions generated in the upper layer are negligible. This is also a convenient configuration in which to examine the effects of dissipation. Geostrophy in the reduced gravity system is given by Eq. (18), while potential vorticity conservation (Eq. 15) is replaced by

$$
v_x = \lambda h - 1, \qquad (46)
$$

where λ is the fractional change in the potential vorticity due to dissipation. The exact functional relationship between λ and the alongstream coordinate is unknown. However, we do know that almost any type of friction will tend to broaden the filament and reduce the magnitude of the negative shear. These correspond to an increase in potential vorticity so that λ will grow with distance downstream. After examining the influence of the bulk parameterization λ, we will consider how the Ekman layer formulations from Section 2b might be applied to filaments.

Combining (18) and (46) yields

$$
h_{xx} - \epsilon^{-1}\lambda h = s_x - \epsilon^{-1}, \qquad (47)
$$

which has the general solution

$$
h = \frac{\epsilon s_x - 1}{\lambda} (c_7 e^{x(\lambda/\epsilon)^{1/2}} + c_8 e^{-x(\lambda/\epsilon)^{1/2}} - 1), \qquad (48)
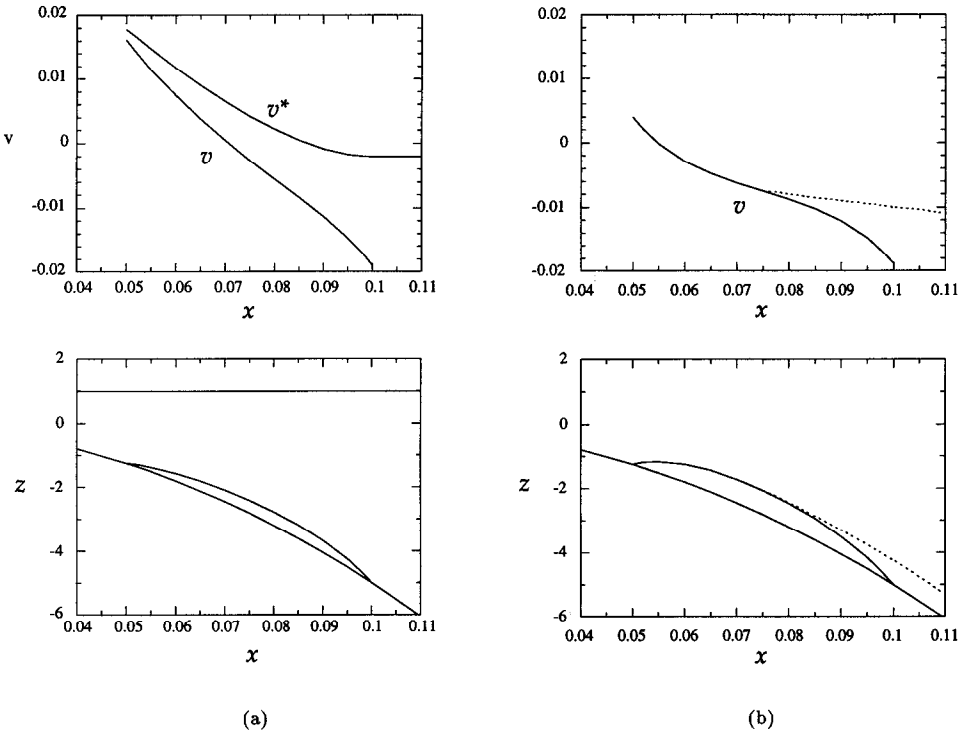$$

(a)   (b)

Figure 11. Dense filament solutions for $\epsilon = 10^{-4}$, $\alpha = 10^3$, $x_4 = 0.05$ and $x_5 = 0.10$. (a) Two-layer solution with $H_4 = 2.25$ and $H_* = H_5 = 6.0$. (b) One and a half layer solution with $H_* = 6.0$ and no dissipation ($\lambda = 1$). The dashed curve represents the deviation from the geostrophic adjustment solution associated with vertical diffusion in a shallow filament which satisfies condition (38) and $F < 1$. (c) Same as (b), except that the dashed curve represents the deviation from the geostrophic adjustment solution associated with vertical diffusion with $F > 1$. This example has $x_E = 0.075$ and $U_E = 8.0 \times 10^{-3} E^{1/2}$. In all plots multiply the x-axis by $\epsilon^{-1/2} = 100$ to obtain units of internal deformation radii.
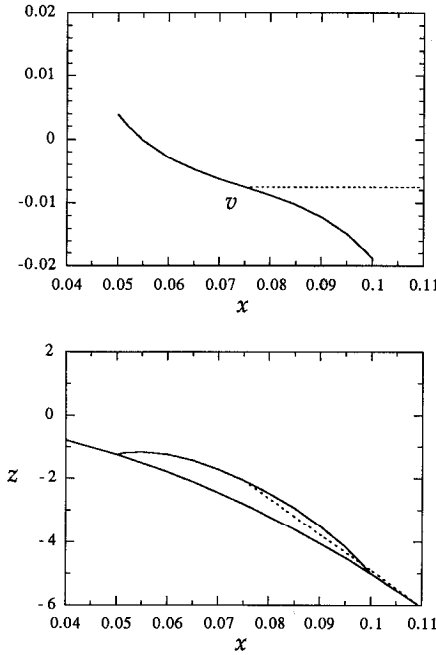
$$v = (\epsilon s_x - 1)\left(\frac{\epsilon}{\lambda}\right)^{1/2} \left(c_7 e^{x(\lambda/\epsilon)^{1/2}} - c_8 e^{-x(\lambda/\epsilon)^{1/2}}\right) - \epsilon s_x, \tag{49}$$

where c_7 and c_8 are constants. Applying boundary conditions (40) and (41) yields

$$c_7 = \frac{1}{e^{x_4(\lambda/\epsilon)^{1/2}} + e^{x_5(\lambda/\epsilon)^{1/2}}}, \tag{50}$$

$$c_8 = \frac{e^{(x_4+x_5)(\lambda/\epsilon)^{1/2}}}{e^{x_4(\lambda/\epsilon)^{1/2}} + e^{x_5(\lambda/\epsilon)^{1/2}}}. \tag{51}$$

In the reduced gravity dissipative system, (18) and (46) also provide an expression for

(c)

Figure 11. (Continued)

the volume flux,

$$\int_{x_4}^{x_5} vh \, dx = B(x_5) - B(x_4),$$ (52)

where

$$B(x) = \frac{1}{\lambda} \left(\frac{1}{2} v^2 + \epsilon \left(h - \int s \, dx \right) \right)$$ (53)

is the Bernoulii function for this system. Volume flux is therefore conserved if B is constant along the streamlines x_4 and x_5. Given the initial values of $B(x_4)$ and $B(x_5)$, (53) can be used to determine x_4 and x_5 as a function of λ.

Before examining the effects of λ, we compare the deep filament solution without dissipation ($\lambda = 1$) represented by the solid curve in Figure 11b to the two layer solution of the same width in Figure 11a. Without potential vorticity constraints on the upper layer, the filament is required to undergo less compression in the vertical and therefore less horizontal shear develops. The shape of the velocity profile is similar to continuously stratified numerical solutions (Ezer and Weatherly, 1990;
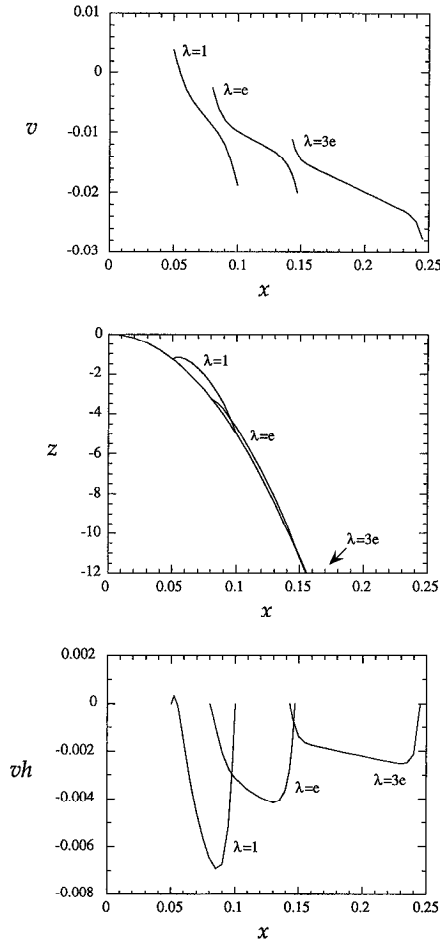
Figure 12. One and a half layer dense filament solutions of velocity (top), depth (center) and transport (bottom) for $\epsilon = 10^{-4}$, $\alpha = 10^3$. Flux is conserved between profiles, while the potential vorticity increases by the factor λ. The depth profile for $\lambda = 3e$ extends from $x_4 = 0.14282$ to $x_5 = 0.24524$, but using this vertical scale is almost indistinguishable from the topographic profile.

Fig. 8), except that the latter decays smoothly to zero at the outer edges of the filament.

The main effects of the parameterized dissipation in the model are to allow the filament to descend the slope, while increasing its width and reducing its mean horizontal shear. Solutions based on relations (48) and (49) for layer depth, velocity and transport are presented in Figure 12 for three values of λ and constant flux. Friction causes the filament to broaden and move down the slope. The speed actually increases in response to the steepening slope and loss of potential energy. However,
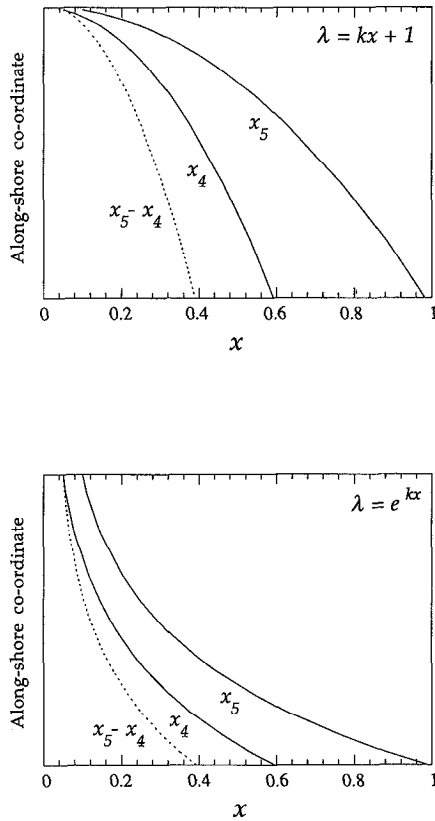
Figure 13. Broadening of a dense filament due to frictional increase in potential vorticity by a factor λ. The total increase shown in these figures is 50 e-folds. The volume flux is conserved, while $\epsilon = 10^{-4}$ and $\alpha = 10^3$. If the potential vorticity increases linearly with distance off-shore (upper) then the rate of descent decreases with distance downstream. However, if the rate of change of potential vorticity is proportional to its local value, then the dense water will descend ever more rapidly down the continental slope (lower).

the horizontal shear across the flow decreases as relative vorticity is dissipated. This is also accompanied by more uniform transport across the filament.

The broadening of the constant flux filament in Figure 12 is plotted against λ in Figure 13. In the first instance (Fig. 13a), potential vorticity increases linearly with distance offshore, while in the second (Fig. 13b), it increases exponentially. While the latter might be preferred on the basis that the level of dissipation should depend on the local value of the potential vorticity, observations of the Norwegian Overflow and the Mediterranian Outflow reveal trajectories which are more consistent with those in Fig. 13a (Smith, 1975). While these flows are influenced by mixing and the detailed topography, the Norwegian Overflow conditions are otherwise consistent with those in Figure 13a. A quantitative comparison with Smith's Figure 7 suggests that the

alongslope *e*-folding distance is around 40 km, so that the length of the vertical axis in Figure 13a is 2000 km or around four non-dimensional units.

The flux-conserving example in Figures 12 and 13 parameterizes the effect of the boundary layer in increasing potential vorticity, but ignores losses in alongslope flux due to Ekman pumping down the slope. This could be improved if the downslope transport were known. One possibility is that the alongslope velocity plateaus at v_N where the shallow layer solution from Section 2b becomes applicable. Matching the velocities given by (37) and (49) indicates that the transition always occur at the midpoint of the filament, $(x_4 + x_5)/2$, as shown by the dashed curve in Figure 11b. It is therefore only relevant to thin filaments which satisfy condition (38) over their entire width. Under these conditions, dissipation is a major influence throughout the filament depth and downslope velocities are comparable to alongslope velocities.

For thicker filaments, the dynamics over the interior are distinct from those in the boundary layer and the more traditional Ekman scaling from Section 2b can be applied. However, in this case, the Ekman transport accumulates over the width of the filament and relation (35) is replaced by

$$v(x_E) = v(x_4) - \left(\frac{2}{E}\right)^{1/2} U_E, \qquad (54)$$

where x_E is again the location at which vertical viscosity becomes important. The layer depth for $x > x_E$ is then given by Eq. (36) with U_Q replaced by U_E and $h(x_E)$ calculated from (48). An example solution is shown in Figure 11c using $U_E = 8.0 \times 10^{-3} E^{1/2}$. This is close to the largest transport which can be maintained far down the slope. For slightly larger U_E, h goes to zero at some point on the slope. This observation can be expressed more generally using (36) with $h > 0$ or

$$U_E < \frac{\epsilon}{x} \left(\frac{E}{2}\right)^{1/2} \left(\int_{x_E}^{x} s \, dx + h(x_E)\right), \qquad (55)$$

for all $x > x_E$. Alternatively, by eliminating U_E between (54) and (55), this can be expressed purely as a constraint on x_E. The specific value of U_E, or equivalently x_E, at a particular alongslope location is determined by the upstream history of the filament and therefore can only be uniquely specified by a three-dimensional model.

It is interesting to compare the cross-stream structure of the bulk parameterization model and the boundary layer models. The major qualitative difference is the pronounced asymmetry which develops between the upslope and downslope sides of the filament in the boundary layer models. This is also evident in numerical models which resolve the bottom boundary layer (Ezer and Weatherly, 1990) and even those with parameterized bottom friction which acts preferentially in shallow regions (Jungclaus and Backhaus, 1994).

c. Laboratory experiments. The configuration used to generate filaments in the laboratory is shown schematically in Figure 14. Dense fluid entered through the base
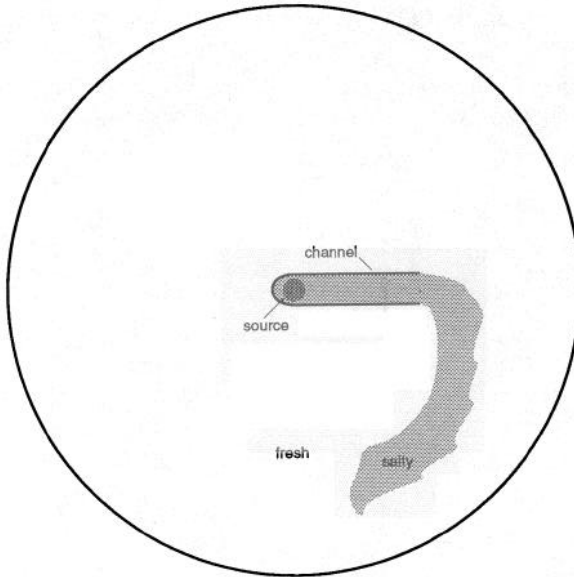
Figure 14. Plan view of the configuration used in the dense filament experiments.

of the cylindrical tank used in the previous experiments. A narrow channel, extending vertically from the bottom to the free surface, carried the intruding fluid out to a prescribed radius where it spread onto the slope. This method produced far less mixing than an isolated source over the slope (Smith, 1977) and therefore allowed smaller density anomalies to be used. This resulted in deeper currents with less dissipation. After leaving the channel, the dense intrusion formed into a filament which flowed azimuthally along the topographic contours. Figure 15 shows the development of an intruding water mass beneath a deep upper layer at a relatively low rotation rate. While most of the flow followed the axisymmetric topographic contours, some of the transport was pumped down the slope within the bottom Ekman layer, causing significant broadening of the flow.

Figure 16 shows azimuthal velocities measured from dye streaks over a radial section 90° from the radius at which the intrusion was introduced. The velocity profile varies very little over the duration of the measurements. It is characterized by strong anticyclonic shear on the upslope side and much weaker cyclonic shear on the downslope side. The alongslope speeds reach a maximum close to the radius of the channel exit and their values typically exeed v_N by an order of magnitude. This suggests that the filament is much deeper than the Ekman layer and should be scaled accordingly.

The theoretical solutions shown in Figure 16 are based on values of x_4, x_5 measured from photographic images similar to Figure 15, and the depth H_1 of the dyed intrusion measured as it first exited the channel. The solid velocity curve corresponds to the $\lambda = 1$ solution. Increasing λ reduces the size of the velocity peaks at the outer
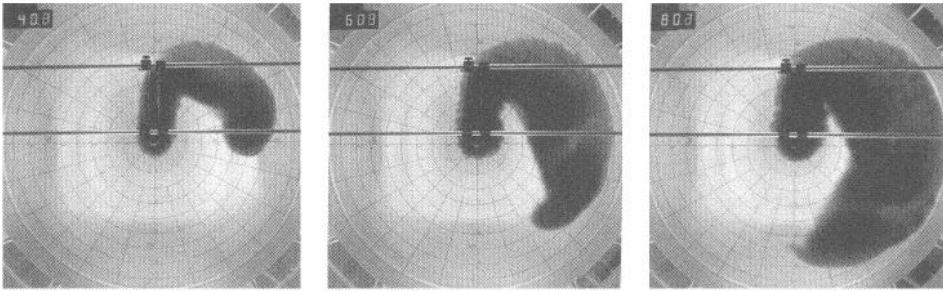
Figure 15. Photographs of the development of an intruding filament. The dense fluid is dyed and the number of rotation periods since the source was turned on is shown in the top left-hand corner. The conditions were $\alpha = 0.25$, $f = 3.0$ s^{-1}, $Q = 2.7$ cm^3 s^{-1} and $\epsilon = 3.8 \times 10^{-3}$, giving an Ekman number of $E^* = 1.5 \times 10^{-3}$ and a Rossby number of $R = 1.3 \times 10^{-3}$. These values fall near the border between Smith's (1977) Class I and Class II flows.

edges and makes the profile more step-like in shape. However, any improvement in the data fit is marginal, suggesting that dissipation has had relatively little influence on this part of the filament. On the other hand, the geostrophic adjustment solution breaks down completely on the downslope side of the filament. Here the velocity structure can be fitted by the Ekman solution from Eq. (54). Selecting $v(x_E)$ to maintain consistency with the experimental data is equivalent to specifying the downslope transport U_E. For the example in Figure 16, U_E decreases with r (due to the circular geometry) from a maximum of 9.2×10^{-4} at $r = 1.4$.

The viscous part of the layer depth solution taken from Eq. (36), predicts a horizontal interface. This is an artifact of the circular geometry, which requires that the downslope transport be inversely proportional to the radius. While $h(r)$ could not be accurately measured experimentally, the total volume flux can be compared to the theoretical estimate for $\int vhdr$. The solution in Figure 16 gives an alongslope flux of 7.5×10^{-3}. Losses through Ekman pumping can also be estimated using the product of the transport in Eq. (54) and the filament pathlength $\pi x_E/2$. This yields an Ekman flux of approximately 2.3×10^{-3}, which gives a combined flux of 9.8×10^{-3}. This is slightly less than half the measured source flux of 2.1×10^{-2}. While some of this discrepancy may be due to detrainment into the upper layer, very substantial losses are also evident within a boundary current which develops along the outer channel wall (Fig. 15). Taking into account such losses, the theoretical flux predictions appear to be reasonably consistent with the laboratory measurements.

The flows in Figures 15 and 16 were relatively stable, allowing meaningful comparisons with the theoretical solutions. However, at higher rotation rates the filaments tended to break-up into a string of eddies as described by Smith (1977). Still further increases in rotation rate helped re-established a more coherent current with anticyclonic eddies aligned along the downslope edge. Leakage of fluid down the slope within the Ekman layer was evident even for these less viscous flows.
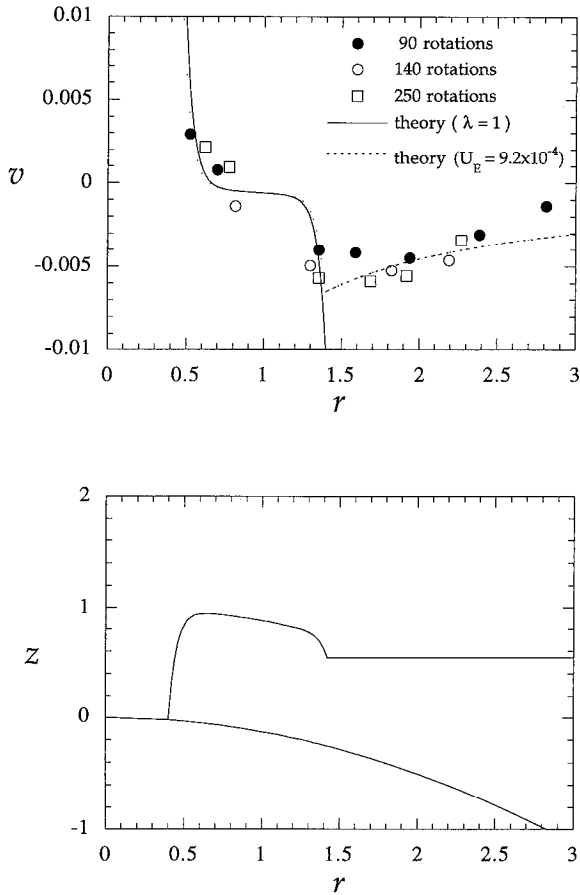
Figure 16. Radial profiles of azimuthal velocity from a dense laboratory filament recorded 90, 140 and 250 rotation periods after the source was turned on. The experimental conditions were $\alpha = 0.25, f = 3.0 \text{ s}^{-1}, Q = 2.7 \text{ cm}^3 \text{ s}^{-1}$ and $\epsilon = 2.37 \times 10^{-3}$, giving $E^* = 9.6 \times 10^{-4}$ and $R = 8.6 \times 10^{-3}$. These are compared with a theoretical solution using $x_4 = 0.4, x_5 = 1.5$, $H_1 = 2.5$ cm and $\lambda = 1$, matched to an Ekman scaling solution with $E = 5.3 \times 10^{-4}$ and $U_E = 9.2 \times 10^{-4}$. The corresponding layer depth solution is also shown.

Ekman pumping also appears to have increased the size of the anticyclonic eddies by driving divergent motions within the boundary layer. For example, the eddy radii were at least a factor of two greater than the free surface experiments of Griffiths *et al.* (1982) and the inviscid estimates of Griffiths *et al.* (1982), Thompson and Young (1989) and Nof (1990). Some distance downstream of the source, the dye pattern also suggests the presence of topographic Rossby waves. These propagate in the same direction as the intrusion and could be generated by the radial outflow at the source or eddy motions further downstream. In either case, they may enhance the stability of the mean flow by carrying away cross-stream momentum.
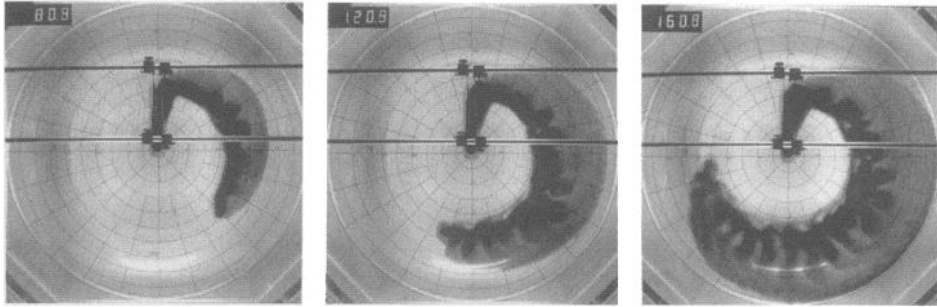
Figure 17. Photographs of the development of a dense filament with $\alpha = 0.25, f = 8.0 \text{ s}^{-1}, Q = 2.7 \text{ cm}^3 \text{s}^{-1}$ and $\epsilon = 3.8 \times 10^{-3}$, giving an Ekman number of $E^* = 2.2 \times 10^{-4}$ and a Rossby number of $R = 5.8 \times 10^{-3}$. This run is significantly less viscous than any of the flows produced by Smith (1977).

The laboratory results for dense filaments can be compared with the flow regimes reported by Smith (1977). These were defined in terms of a second Ekman number,

$$E^* = \frac{g\epsilon\nu}{f^2Q}, \tag{56}$$

and a Rossby number,

$$R = \left(\frac{g^3\epsilon^3s^4}{f^5Q}\right)^{1/2}, \tag{57}$$

where s is taken here to be the slope where the dense fluid exits the channel. Smith's most inviscid flows were referred to as Class I and fell within the range $10^{-3} < E^* < (R, 10^{-2})$. They consisted of a string of eddies interconnected by a strongly meandering jet. Our experiments yielded almost identical behavior within this regime and therefore are not shown. The slightly more viscous flow shown in Figure 15 falls near the boundary between Smiths Class I and Class II (i.e. $R \simeq E^* < 10^{-2}$). While the general structure is similar to that described for Class II, there was no evidence for the small-scale instability described by Smith (1977). Finally, flows such as that in Figure 17 with $E^* < 10^{-3} < R < 10^{-2}$ were less viscous than any described by Smith (1977). They revealed a new mode of behavior, in which eddies formed along the downslope edge, but without the very strong meandering associated with Class I flows. However, like the previous regimes, most of the downslope transport appeared to be concentrated within the bottom boundary layer.

4. Implications for deep water formation around Antarctica

Descending water masses are particularly significant around the Antarctic continental margin where they supply much of the deep water and most of the bottom

water for the worlds oceans. They also have a strong influence on biological productivity by replenishing deeper waters with oxygen and nutrients, while replacing subducted shelf water with upwelled water which is often rich in krill larvae. While observations in these regions are relatively sparse, preliminary comparisons can be made with some aspects of the theoretical and laboratory models.

The Antarctic Slope Front (Fig. 2) is a robust feature along much of the Antarctic shelf-break. The subsurface flow is characterized by strong westward velocities and significant shear (Keys *et al.*, 1990). The outcropping tends to be concentrated close to the ice cover, (suggesting small values of x_2), so that there is often little surface evidence of the front. This is consistent with both the laboratory experiments and theoretical solutions, which suggest that the inviscid part of the front may be effectively trapped on the shelf. In the case of the solution in Figure 3a, the width of the front is less than two internal deformation radii, $(g\epsilon H_1)^{1/2}/f$, and reaches maximum speeds approaching the wave speed $(g\epsilon H_1)^{1/2}$. This width is consistent with data from Figure 2, however, the inviscid solutions overestimate observed velocities by up to a factor of two (Jacobs, 1991).

Frictional effects beyond the Antarctic shelf-break are revealed by tracers such as salinity, dissolved oxygen, silicate and phosphate, which appear to have been carried down slope within the bottom boundary layer. The density characteristics of these waters led Jacobs (1991) to conclude that much of the deep ocean is ventilated by waters descending from the bottom boundary layer beneath the Antarctic Slope Front. If this is true, then the dynamical balance near the leading edge of the front is likely to be similar to that in the viscous theory and laboratory experiments. Qualitatively, the front will move offshore and the alongslope velocity will increase only until the Ekman flux approximately balances the production of new dense water. The structure of the viscous region of the flow will depend on the magnitude of F, which in terms of dimensional variables becomes

$$F = \frac{U_Q}{g\epsilon s} \left(\frac{f^3}{\nu}\right)^{1/2}. \tag{58}$$

Using scales of $f \sim 10^{-4} \, \text{s}^{-1}$, $\epsilon \sim 10^{-4}$, $s \sim 10^{-2}$, $\nu \sim 10^{-2} \, \text{m}^2 \, \text{s}^{-1}$ and $U_Q \sim 1 \, \text{m}^2 \, \text{s}^{-1}$, gives $F \sim 1$. Because ν is poorly constrained, any value of F near unity makes it difficult to differentiate between the two regimes. However, under such conditions the dimensional alongslope velocities,

$$v_E = -\left(\frac{2f}{\nu}\right)^{1/2} U_Q, \tag{59}$$

$$v_N = -\frac{g\epsilon s}{f}, \tag{60}$$

both give realistic estimates of around $0.1 \, \text{m s}^{-1}$.

Hydrographic data may be used more directly to identify the relevant regime. For example, Figure 2 reveals that isopycnals are significantly steeper than the topography within 10 km of the shelf break, suggesting that the normal Ekman scaling applies in this region. Further offshore, parts of the slope are steeper and some of the transport may have been lost through detrainment. These factors tend to reduce F and thus favor a uniform depth solution. While not obvious in the density structure, the corresponding salinity section reveals a layer of relatively constant depth extending through the 2000 m isobath (Jacobs, 1991). The depth of this layer collapses to around 50 m over the steeper regions, which is consistent with estimates based on Eq. (38).

While there is some evidence of filament-like structures to the west of the Ross Sea (Gordon and Tchernia 1972; Carmack and Killworth, 1978), currently available data sets do not allow a detailed comparison with the theory. There is also no documentation of the transition of slope front water into filament structures. If the slope front drains through the bottom Ekman layer, then it could only form a new bounded geostrophic front by re-accumulating along deeper topographic features. A simpler mechanism would be topographic steering of the shelf water down the slope by features such as submarine ridges and canyons, which are relatively common along the Antarctic continental margins.

5. Conclusion

The slope front theory indicates that dense water undergoes geostrophic adjustment close to the source, where the offshore Ekman transport grows due to interior horizontal shear. When the Ekman transport carries most of the new dense water production, the velocity plateaus. While the maximum alongslope velocity is always determined by a balance between dense water production and Ekman transport, the detailed scaling depends on the parameter F. This is confirmed by results from the laboratory experiments.

Extending the theory to the case of deep filaments, indicates that friction will tend to broaden these flows, reduce their shear, and move them down the continental slope into the deeper ocean. Solutions which explicitly include boundary layer dynamics reveal that Ekman transport grows over the upslope side of the filament due to the shear associated with geostrophic adjustment. Both the Ekman transport and alongslope velocity then plateau on the downslope side. However, the point at which this transition occurs can only be uniquely determined by a three-dimensional model. These results have again been shown to be quantitatively consistent with those from laboratory experiments.

For both slope fronts and dense filaments, downslope transport was concentrated within the bottom Ekman layer throughout the experimental parameter range. This suggests that such processes may also make a major contribution to the production of deep water in the ocean. However, there still remains a question as to what fraction

of dense water descends the continental slope as dense filaments compared to bottom boundary layers. While the laboratory experiments tend to support a boundary layer mechanism, the actual balance will probably depend strongly on topographic details such as the presence of submarine canyons and seamounts (Jungclaus and Backhaus, 1994). Other major issues which have not been addressed here are the influences of turbulent mixing (Price and Baringer, 1994) and strongly stratified environments.

REFERENCES

Carmack, E. C. and P. D. Killworth. 1978. Formation and interleaving of water masses off Wilkes Land, Antarctica. Deep-Sea Res., *25,* 357–369.
Chapman, D. C. and S. J. Lentz. 1994. Trapping of a coastal density front by the bottom boundary layer. J. Phys. Oceanogr., *24,* 1464–1479.
Condie, S. A. 1993. Formation and stability of shelf-break fronts. J. Geophys. Res., *98,* 12405–12416.
Condie, S. A. and M. Kawase. 1993. Models of abyssal circulation in basins separated by a mid-ocean ridge. J. Mar. Res., *50,* 421–440.
Csanady, G. T. 1988. Ocean currents over the continental slope. Adv. Geophys., *30,* 95–203.
Ezer, T. and G. L. Weatherly. 1990. A numerical study of the interaction between a cold jet and the bottom boundary layer in the ocean. J. Phys. Oceanogr., *20,* 800–816.
Garrett, C., P. MacCready and P. Rhines. 1993. Boundary mixing and arrested Ekman layers: Rotating stratified flow near a sloping boundary. Ann. Rev. Fluid Mech., *25,* 291–323.
Gawarkiewicz, G. and D. C. Chapman. 1992. The role of stratification in the formation and maintenance of shelf-break fronts. J. Phys. Oceanogr., *22,* 753–772.
Gordon, A. L. and P. Tchernia. 1972. Waters of the continental margin off Adelie Coast, Antarctica. Antarct. Res. Ser., *19,* 59–69.
Griffiths, R. W. 1986. Gravity currents in rotating systems. Ann. Rev. Fluid Mech., *18,* 59–89.
Griffiths, R. W., P. D. Killworth and M. E. Stern. 1982. Ageostrophic instability of ocean currents. J. Fluid Mech., *117,* 343–377.
Hsueh, Y. and B. Cushman-Roisin. 1983. On the formation of surface to bottom fronts over steep topography. J. Geophys. Res., *88,* 743–750.
Jacobs, S. S. 1991. On the nature and significance of the Antarctic Slope Front. Mar. Chem., *35,* 9–24.
Jacobs, S. S., A. F. Amos and P. M. Bruckhausen. 1970. Ross Sea oceanography and Antarctic bottom water formation. Deep-Sea Res., *17,* 935–962.
Jungclaus, J. H. and J. O. Backhaus. 1994. Application of a transient reduced gravity plume model to the Denmark Strait Overflow. J. Geophys. Res., *99,* 12,375–12,396.
Kawase, M. 1987. Establishment of deep ocean circulation driven by deep water production. J. Phys. Oceanogr., *17,* 2294–2317.
Keyes, H., S. S. Jacobs and D. Barnett. 1990. The calving and drift of iceberg B-9 in the Ross Sea, Antarctica. Antarct. Sci., *2,* 243–257.

Journal of Marine Research [53, 6

Killworth, P. D. 1983. Deep convection in the world ocean. Rev. Geophys. Space Phys., *21*, 1–26.

MacCready, P. 1994. Frictional decay of abyssal boundary currents. J. Mar. Res., *52*, 197–217.

MacCready, P. and P. B. Rhines. 1991. Buoyant inhibition of Ekman transport on a slope and its effect on stratified spin-up. J. Fluid Mech., *223*, 631–661.

—— 1993. Slippery bottom boundary layers on a slope. J. Phys. Oceanogr., *23*, 5–22.

Nagata, Y., R. Kimura, H. Honji, Y. Yamazaki, K. Kawaguchi and T. Hosoyamada. 1993. Laboratory experiments of dense water descending on continental slope, *in* Deep Ocean Circulation, Physical and Chemical Aspects, T. Teramoto, ed., Elsevier, Amsterdam.

Nof, D. 1990. The breakup of dense filaments. J. Phys. Oceanogr., *20*, 880–889.

Nof, D., N. Paldor and S. van Gorder. 1991. Abyssal gyres. Geophys. Astrophys. Fluid Dyn., *58*, 173–196.

Ou, H. W. 1983. Some two-layer models of the shelf-slope front: Geostrophic adjustment and its maintenance. J. Phys. Oceanogr., *13*, 1798–1808.

Pedlosky, J. 1987. Geophysical Fluid Dynamics, Springer Verlag, New York.

Price, J. F. and M. O. Baringer. 1994. Outflows and deep water production by marginal seas. Prog. Oceanogr., *33*, 161–200.

Shaw, P. T. and G. T. Csanady. 1983. Self-advection of density perturbations on a sloping continental shelf. J. Phys. Oceanogr., *13*, 769–782.

Smith, P. C. 1975. A streamtube model for bottom boundary currents in the ocean. Deep-Sea Res., *22*, 853–873.

—— 1977. Experiments with viscous source flows in rotating systems. Dyn. Atmos. Ocean., *1*, 241–272.

Stommel, H. and A. B. Arons. 1972. On the abyssal circulation of the world ocean-V. The influence of bottom slope on the broadening of inertial boundary currents. Deep-Sea Res., *19*, 707–718.

Symonds, G. and R. Gardiner-Garden. 1994. Coastal density currents forced by cooling events. Cont. Shelf Res., *14*, 143–157.

Thompson, L. and W. R. Young. 1989. An upper bound on the size of sub-mesoscale coherent vorticies. J. Phys. Oceanogr., *19*, 233–237.

Wright, D. G. and A. J. Willmott. 1992. Buoyancy-driven abyssal circulation in a circumpolar ocean. J. Phys. Oceanogr., *22*, 139–154.

Wright, L. D., W. J. Wiseman Jr., Z.-S. Yang, B. D. Bornhold, G. H. Keller, D. B. Prior and J. N. Suhayda. 1990. Processes of marine dispersal and deposition of suspended silts off the modern mouth of the Huanghe (Yellow River). Cont. Shelf Res., *10*, 1–40.